Experimental and theoretical determination of the low-loss electron energy loss spectroscopy of $LiMn_2O_4$

F. Espinosa-Magaña, L, Alvarez-Contreras, M.T. Ochoa-Lara, S.M. Loya-Mancilla, A. Aguilar-Elguezabal.

Abstract

The dielectric properties of cubic spinel-type $LiMn_2O_4$, used as cathode material in lithium ion secondary batteries, are studied by analyzing the low-loss region of the electron energy loss spectroscopy (EELS) spectrum in a transmission electronmicroscope. A comparison of experimental EELS spectra and ab initio density-functional theory calculations (WIEN2k code) within the generalized gradient approximation (GGA) is presented. The origins of interband transitions are identified in the electronic band structure, by calculating the partial imaginary part of the dielectric function and the partial density of states of Li, Mn and O. Good agreement with experimental spectra is observed which allowed interpreting main features of the EELS spectrum.

Keywords: EELS, Ab initio, Electronic structure, $LiMn_2O_4$, Dielectric function

Introduction

The use of rechargeable batteries has become a standard for mobile applications, with $LiCoO_2$ as themost common material used for the cathode since many years. In spite of this, high costs incurred as a result of cobalt toxicity have stimulated investigation into cheaper, more environmentally friendly materials as alternatives to cobalt. One of the most promising materials with these traits is spinel $LiMn_2O_4$ (Na et al.,

2005; Yun-Sung et al., 1998; Hwang et al., 2001;Wang et al., 2003). Several methods have been employed for synthesizing $LiMn_2O_4$. Such methods include solid-state reaction of manganese and lithium precursors at high temperatures (Siapkas et al., 1998; Tao et al., 2006), pulsed laser deposition (Kuwata et al., 2006; Tang et al., 2006), spray drying (Wuet al., 2005; Tu et al., 2007) and a combustion method (Rojas et al., 2006; Cheng-Zhang and Fey, 2006). However, the method which is most widely employed is the sol–gel route (Jeong et al., 2006; Fu et al., 2005; Kwang and Jang, 2007). Cubic spinel oxides derive their properties from the large region of stability they exhibit in respect to lithium content. The intercalation mechanism of lithium is the reason lithium is used as the electrode in rechargeable batteries.

Although numerous experimental works have been dedicated to determining the electrochemical characteristic of lithium cells, recent studies (Grechnev et al., 2002, and references therein) have been aimed at investigating the structural, electronic, magnetic, and optical properties of spinel-type lithium manganese oxides, a basic understanding of the electronic structure and chemical bonding of electrode materials, which underlies the electrochemical behavior of the battery, is necessary for the development of advanced electrode materials.

Electron energy loss spectroscopy (EELS) has been widely used for studying materials composition and electronic structure (Egerton, 1996; Ahn, 2004; Brockt and Lakner, 2000). The interactions of fast electrons with the specimen result in electrons being excited into unoccupied energy levels within the conduction band as well as collective excitation of valence electrons. When a spectrum is obtained by analyzing energy loss due to incident electrons, the region up to ~50 eV is dominated by collective

excitation of valence electrons (plasmon) and interband transitions. With greater energy loss, ionization edges occur due to the core electrons being excited into the conduction band. Interband transitions are caused by electrons being excited within the valence band and then entering the empty states of conduction bands. Therefore, these energy losses can be identified as transitions in a band structure model.

From the dielectric theory, it is possible to relate the experimental single scattering distribution S(E), to the energy loss function Im(-1/ε) (Egerton, 1996) by:

$$S(E) = \frac{I_0 t}{\pi a_0 m_0 v^2} \mathrm{Im}\left[-\frac{1}{\varepsilon(q,E)}\right] \ln\left[1+\left(\frac{\beta}{\theta_E}\right)^2\right] \qquad (1)$$

where $\varepsilon(q,E) = \varepsilon_1 + i\varepsilon_2$ is the complex dielectric function at energy loss E and momentum transfer q, a_0 the Bohr radius, m_0 the electron rest mass, v the electron beam velocity, θ the scattering angle and $\theta_E = E/(\gamma m_0 v^2)$ is the characteristic scattering angle, γ is the relativistic factor, I_0 is the zero-loss intensity, t the specimen thickness and β is the collection semi-angle.

While peak positions with low-energy losses in the energy loss spectrum are strongly influenced by plasmon volume and positions of other excitations, the energy loss spectrum cannot be directly associated to interband transitions. Nevertheless, the imaginary part of the dielectric function $\varepsilon_2(E)$ can be associated to interband transitions. The real and imaginary parts of the dielectric function can be obtained from the energy loss function through Kramers–Kronig analysis.

It has been recognized that EELS can be used to probe the electronic structure of materials. It has been widely applied as fingerprint studies, allowing the identification of phases by comparing well-known spectra. In the high-loss region, analysis of the first

10 eV of the spectra after the ionization edge (ELNES) can give information about the oxidation state, absolute energy position, and local symmetry via d level splittings in transition metal elements and orbital hybridization. The low-loss region can provide information about composition and electronic structure as well as optical properties although it has not been as widely applied as ELNES. The reason is due to the well-known fact that low-losses are caused by all possible transitions between the valence band and conduction band. The valence band is made up of dispersed levels as opposed to almost flat core levels and the interpretation of EELS is a priori more difficult.

On the other hand, theoretical investigations have previously been carried out to reveal basic features on the electronic structure for the lithiated manganese oxides by means of linear-muffin-tin orbital (LMTO-ASA) (Berg et al., 1999), full-potential (FP) LAPW (Singh, 1997) and pseudopotential (Aydinol et al., 1997; Mishra and Ceder, 1999; Van der Ven et al., 2000) calculations. However, only few of them are devoted to interpreting low-loss EELS spectra. Recently (Mauchamp et al., 2006), studied spinel $LiMn_2O_4$ over the low-loss region, with both EELS and ab initio calculations, but they focused on the Li K edge, which lies at ~55 eV energies.

In this work, we performed a thorough study of the low-loss energy loss region of the spinel $LiMn_2O_4$ both experimentally (EELS) and theoretically by means of the WIEN2k code (Blaha et al., 2001, 1990). Our goal in performing the ab initio band structure calculations was to aid in the interpretation of the low-loss spectra.

Experimental

Spinel $LiMn_2O_4$ powders were synthesized by the sol–gel method using citric acid as the chelating agent. Stoichiometric amounts of lithium acetate, manganese acetate, and citric acid were thoroughly mixed and dissolved in de-ionized water. The solution was then continuously stirred under heat at 60 °C in order to obtain complete homogeneity; the pH was kept at 5. Fourteen milliliters of 1 M citric acid were added to the homogenous solution, drop by drop, and a smooth gel was obtained. The synthesized samples were dried overnight in an oven at 85 °C in order to remove moisture and to obtain a dried mass. The dried mass was ground and calcinated at 950 °C for 10 h at a rate of 1 °C/ min per 4 h. Samples were analyzed by X-ray diffractometry (XRD) to make sure a spinel-type structure was obtained.

Thin specimens suitable for electron microscopy were prepared by placing clean, dry crushed powders onto commercial holey carbon-coated copper grids. Electron energy loss spectra were obtained using a Gatan Parallel Electron Energy Loss Spectrometer (PEELS model 766) attached to a Philips CM-200 transmission electron microscope. Spectra were acquired in diffraction mode with 0.2 eV/ch dispersion, an aperture of 2 mm and a collection semi-angle of about 2.7 mrad. The resolution of the spectra was determined by measuring the full width at half-maximum (FWHM) of the zero-loss peak which was typically close to 1.0 eV, when the TEM was operated at 200 kV. EELS spectra were corrected for dark current and readout noise. The channel to channel gain variation was minimized by normalizing the experimental spectrum with an independently obtained gain spectrum of the spectrometer. Next, all spectra were deconvoluted by the zero-loss peak (ZLP) recorded in a hole of the grid to obtain single scattering distributions S(E).

Calculation details

Self-consistent band structure calculations were performed using density-functional theory (DFT) with the full-potential linearized augmented plane-wave (FLAPW) method as implemented in the WIEN2k code (Blaha et al., 2001, 1990). Exchange and correlation were treated by using the generalized gradient approximation (GGA) for the potential. The core states were treated in a fully relativistic fashion. The wave functions within the muffin-tin spheres were expanded in spherical harmonics with an angular momentum up to l = 10. Additional local orbital extensions were used to avoid linearization errors. Nonspherical contributions to the charge density and the potential within the muffin-tin spheres were considered up to l_{max} = 4. In the interstitial region, plane waves with reciprocal lattice vectors of up to G = 10 were included and the plane-wave cut-off ($R_{MT}K_{max}$) was set to 9. For each compound, the muffin-tin radii were chosen as 1.86, 1.95 and 1.73 a.u. for Li, Mn and O, respectively. Self-consistency was considered to be achieved when the total energy variation from iteration to iteration did not exceed 10^{-5} Ry, on a mesh containing 165 k-points in the irreducible Brillouin zone (IBZ).

The dielectric function can be obtained from the OPTIC Program of the WIEN2k code, (Ambrosch-Draxl and Soto, 2006) allowing for comparison with experiment:

$$\varepsilon_{2ii}(\omega) = \frac{4\pi^2 e^2}{m^2\omega^2 V}\sum_{v,c,k}\left|\langle\psi_k^v|\, p_i|\psi_k^c\rangle\right|^2\delta(E_{\psi_k^c} - E_{\psi_k^v} - \hbar\omega) \qquad (2)$$

Matrix elements are calculated from electron states and then the integral over the irreducible Brillouin zone is calculated in order to obtain the imaginary part of the

dielectric function. Afterwards a Kramers–Kronig analysis is performed in order to obtain the real part of the dielectric function e1 and finally the energy loss function Im(-1/ε).

The crystal structure of the cubic spinel $LiMn_2O_4$ has been widely studied experimentally, having a face-centered Bravais lattice with space group Fd-3m. The lattice constant is 8.2455Å, taken from the experimental results (Akimoto et al., 2004). The unit cell contains two formula units with the Li sitting at (0.125, 0.125 and 0.125), the Mn at the body center (0.5, 0.5 and 0.5) and the oxygen at (0.2634, 0.2634 and 0.2634).

Optical properties were calculated on a mesh which had 1240 kpoints on the irreducible part of the Brillouin zone due to the fact that many points are needed for carrying out optical calculations.

Results and discussion

Fig. 1 shows the experimental EELS spectrum for $LiMn_2O_4$, as well as calculated energy loss function Im[-1/ε]. Experimental spectra were deconvoluted with the zero-loss spectrum, which were acquired from a hole in the sample. The zero-loss peak was not removed due to the fact that is well known that this process introduces artifacts in derived results. However, it is well known that multiple scattering may raise the intensity on the higher energy side of the bulk plasmon peak. When we continue one step ahead and remove multiple scattering, no significant differences are observed in the shape and intensity of the plasmon peak, but some features in the spectrum are diminished. The inset graph in Fig. 1, shows the deconvoluted spectrum with and without multiple scattering removed. Calculated and experimental featured peaks are labeled as a–j and B–D, F, respectively. Energy peak positions are summarized in Table 1.

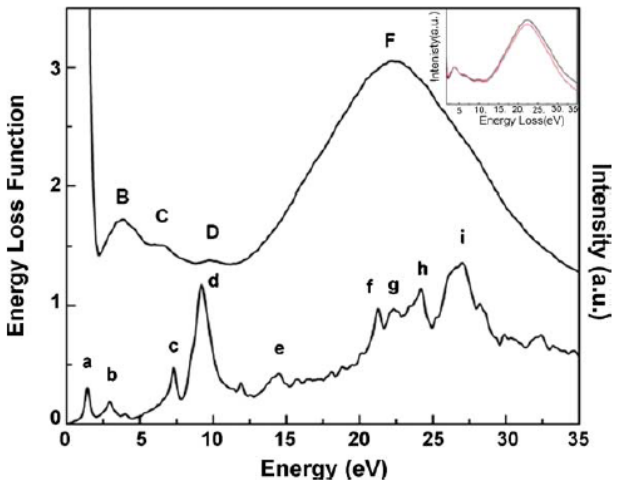

Fig. 1. Comparison between experimental (upper) and calculated (lower) energy loss function for $LiMn_2O_4$. The ZLP has not been removed from the experimental spectrum and the calculated spectrum has been broadened by 0.1 eV. The inset graph shows the deconvoluted spectrum with (red) and without (black) multiple scattering removed. (For interpretation of the references to color in this figure legend, the reader is referred to the web version of the article.)

The comparison between experimental and calculated spectra is very good indeed, as far as peak positions are concerned, when the relatively low resolution attained in experimental results (~1.0 eV) is taken into account. Peaks labeled B–D and F in the experimental spectrum compare well with labeled peaks b–d and f for calculated spectra. Peaks g–i, which do not have an experimental counterpart deserve special attention. It is important to point out that if it were possible to interpret and justify the presence of these peaks, then calculated electronic structure would be validated and would make possible the inference of electronic properties in great detail with a resolution that is presently impossible to attain in the laboratory.

To start with, we analyze the origin of all the well defined a–I characteristic peaks that were obtained from calculations. Fig. 2 shows the real part of the dielectric function, where we have identified the points P1, P2, P3 and P4, which have zero-crossing with the energy axis with a positive slope, indicating the presence of well defined plasmon

signals. Plasmon at P1 comes from the Drude term, related to free electrons and corresponds to point a in Fig. 1, with an energy of 1.4 eV. Looking at Table 1 we can identify the other three plasmon signals in the energy loss function plot, with energies 7.3, 9.2 and 21.3 eV, respectively, with corresponding points c, d and f in Fig. 1. The remaining points b, e and g–i come from interband transitions and can be identified with the peaks in the ε_2 vs. E plot.

Table 1
Experimental and calculated peak positions in the energy loss function.

Peak label (calculated)	Peak position (calculated), eV	Peak label (experimental)	Peak position (experimental), eV
a	1.4	–	–
b	3.0	*B*	3.8
c	7.3	*C*	6.0
d	9.2	*D*	9.8
e	14.5	–	–
f	21.3	*F*	22.2
g	22.3	–	–
h	24.2	–	–
i	27.0	–	–

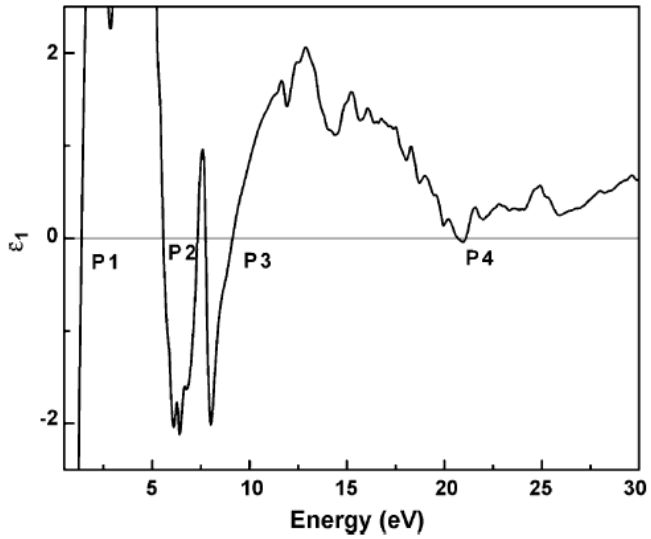

Fig. 2. Calculated real part of the dielectric function. Zero-crossings with positive slope show the presence of well defined plasmons.

Fig. 3 shows the calculated imaginary part of the dielectric function. Well-defined maxima are labeled as I1, I2, I3, I4, I5 and I6 and correspond to interband transitions at 2.5, 5.1, 7.8, 13.5, 21.7 and 25.5 eV, respectively. Peaks at 21.7 and 25.5 eV in the ε_2 vs. E plot give rise to prominent peaks h (24.2 eV) and I (27.0 eV) in the energy loss function of Fig. 1 and are responsible for the apparent shift of the experimental plasmon to higher energy at 22.2 eV. Peak i is actually formed by a double peak with energies at 25.0 and 25.5 eV in ε_2. These peaks are difficult to justify in terms of the experimental results because they cannot be thought of as hidden by the experimental broadening. The cause of these peaks can be sought after by calculating the partial imaginary part of the dielectric function, as implemented in WIEN2k. This allows using a smaller set of energy bands from where the construction of the partial ε_2 could be made up and which arise from all possible combinations of the valence and conduction bands of the chosen set. Fig. 4a–c shows the results of the partial ε_2 calculations that were carried out by tracing peaks I5 and I6 and by choosing three sets of combinations for band to band transitions. Fig. 4a shows that the peak at 24.2 eV in Im(-1/ε), which arises from the interband transition at 21.7 eV for ε_2 is mainly due to transitions between band 47 and band 97 where the peak is well defined; whereas it almost disappears when transitions from bands 47 to 96 and 48 to 97 are considered. In a similar manner, Fig. 4b and c shows that the double peak around 27.0 eV in Im(-1/ ε) was caused by interband transitions at 25.0 and 25.5 eV in ε_2 and mainly come from transitions between band 50 and band 106 and between band 45 and band 107, where the peaks are well defined.

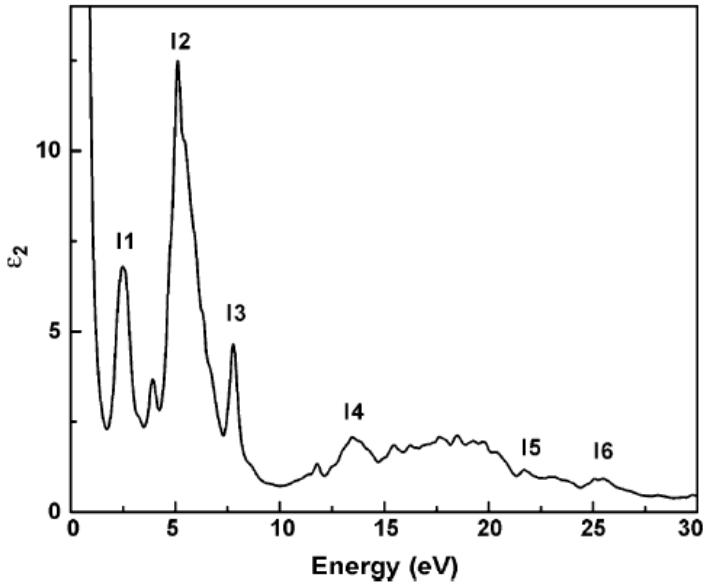

Fig. 3. Imaginary part of the dielectric function. Maxima show interband transition where absorption takes place.

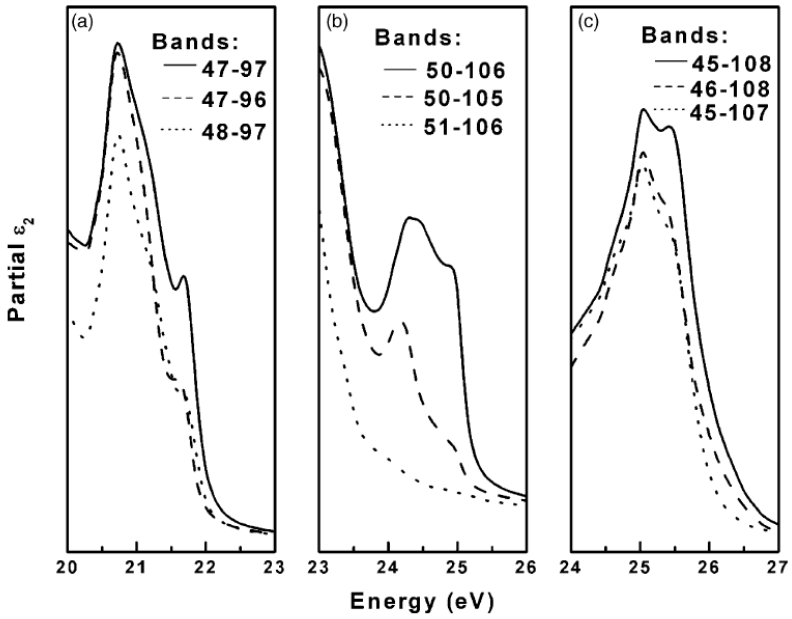

Fig. 4. Calculated partial imaginary part of the dielectric function.

Fig. 4b shows that the intensity of the 25.0 eV decreases when band 106 is eliminated (bands 50–105) and disappears when band 50 is absent (bands 51–106). Fig. 4c shows that peak at 25.5 eV for ε_2 is caused by transitions between bands 45 and

108; furthermore, if the partial ε_2 is calculated by using the transitions between bands 46 and 108 or between bands 45 and 107, the peak at 25.5 has disappeared.

The three peaks which were considered were caused by electrons initially located in energy bands 45–50 making transitions to bands 97–108. Bands 45–50 lie in the energy range between -3.7 and -2.2 eV and bands 97–108 in the energy range 18.4–24.3 eV. The two energy intervals in the partial density of states plot can be located as shown in Fig. 5.

Band 47 is composed mainly by O p (76%) and Mn d (16%) orbitals, while band 97 has Li p (41%) and Mn p (32%) orbitals. If only dipolar transitions are allowed, peak at 21.7 eV in ε_2 is dominated by transitions from Mn d to Li p and Mn p.

Band 50 contains an overwhelming majority of O p states (82%) and band 106 is mainly composed by Li p (55%) and Mn d (15%) orbitals. Therefore, peak at 25.0 eV in ε_2 comes then from transitions from O p to Mn d states.

Finally, band 45 is mainly composed of O p orbitals (72%) and Mn d (19%) and band 108 contains Li p (48%) and Mn d (24%). The peak at 25.5 eV in ε_2 is mainly caused by transitions from O p to Mn d states and from Mn d to Li p states.

The peak at 22.3 eV in the energy loss function, labeled g in Fig. 1, comes from allowed-dipole transitions between d states below the Fermi energy and p states above the Fermi energy and the peak h at 24.2 eV arises by transitions from p states below the Fermi energy to d states above the Fermi energy. The broadened experimental maximum at 22.2 eV, which could erroneously be attributed a plasmon character, is actually due to peaks f–i in theoretical calculations and thus shift the spectrum to higher energies. The most intense calculated peak is at about 27 eV in Fig. 1. If it were present

in the experimental spectrum, it would shift the maximum towards higher energies, close to 27 eV. Nevertheless, this shift is definitely not observed by EELS; thus this is a shortcoming in the calculations.

Within the random phase approximation (RPA), an important issue in the calculation of the dielectric function and thus of the energy loss function and the imaginary part of the dielectric function, is the inclusion of the crystal local-field effects (LFE). The microscopic fields induced in the material by the external electric fields of the fast electrons in an EELS experiment and arising from the inhomogeneities of the electronic density of the material were proven to have a dramatic effect on the calculation of the plasmon in certain materials. In the OPTIC package, LFE are absent, and these effects can give rise to discrepancies in experimental data under certain circumstances.

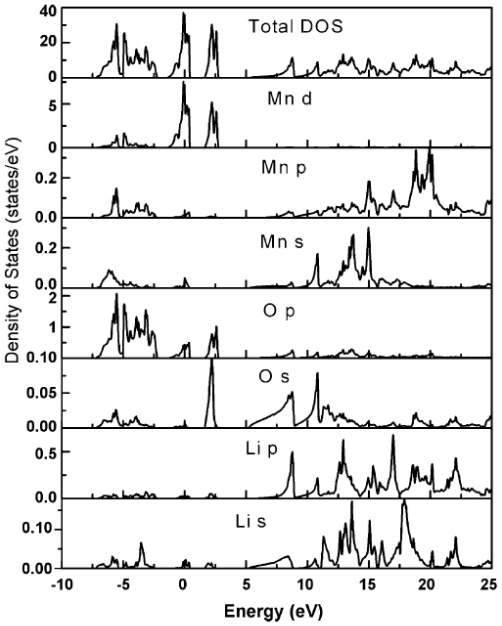

Fig. 5. Calculated total and partial site-projected density of states. The Fermi energy has been chosen at the origin.

Although some authors believe that localfield effects are only relevant at relatively high energies (Vast et al. 2002), Gurtubay et al. (2004), reported ab initio time-dependent density-functional calculations of rutile TiO_2 and observed large crystal local-field effects at low energies. In $LiMn_2O_4$, Mn oxidation states come from mixed Mn^{3+}–Mn^{4+} cations randomly distributed in equal amounts over the octahedral sites in the spinel structure, thus causing a locally inhomogeneous electron density in the material. These inhomogeneities could be the source of an appreciable influence of LFE on the calculated i peak. By taking this peak aside, a good correlation between our experimental and calculated spectra was obtained, in spite of the fact that manganese oxides are usually considered strongly correlated systems, and as such, are difficult to be appropriately treated by DFT band theory.

Conclusions

The electronic structure of sol–gel synthesized spinel-type $LiMn_2O_4$ has been studied by low-loss transmission Electron Energy Loss Spectroscopy and ab initio calculations. Good agreement was observed between experimental and calculated spectra, as far as energy peak positions of plasmons and interband transitions is concerned, except for the double peak at 25.0 and 25.5 eV in the imaginary part of the dielectric function, which appears as a double peak at ~27.0 eV in the calculated energy loss function and not in EELS spectra. This peak could be attributed to local-field effects not included in the OPTIC package of the WIEN2k code. Although the DFT approach has obvious limitations in describing the excited electronic states, in many cases the calculated optical spectra appear to be in agreement with experimentation and provide further insight into the electronic structure of complex oxides.

Acknowledgement

The authors acknowledge the financial support by CONACYT and Gobierno del Estado de Chihuahua, through the project CHIH- 2006-C02-58660.

References

1. - Ahn, C.C., 2004. Transmission Electron Energy Loss Spectrometry in Materials Science and the EELS Atlas. WILEY–VCH Verlag GmbH & Co. KGaA Weinheim.
2. Akimoto, J., Takahashi, Y., Kijima, N., Gotoh, Y., 2004. Single-crystal X-ray structure analysis of the low temperature form of LiMn2O4. Solid State Ionics 172, 491–494.
3. Ambrosch-Draxl, C., Soto, J.O., 2006. Linear optical properties of solids within the full-potential linearized augmented planewave method. Comput. Phys. Commun.175, 1–14.
4. Aydinol, M.K., Kohan, A.F., Ceder, G., Cho, K., Joannopoulos, J., 1997. Ab initio study of lithium intercalation in metal oxides and metal dichalcogenides. Phys. Rev. B 56, 1354–1365.
5. Berg, H., Göransson, K., Nola¨ng, B., Thomas, J.O., 1999. Electronic structure and stability of the LixMn2O4 (0 < x < 2) system. J. Mater. Chem. 9, 2813–2820.
6. Blaha, P., Schwarz, K., Madsen, G.K.H., Kvasnicka, D., Luitz, J.2001., 2001. Computer code WIEN2k. Technische Universita¨ t Wien, Austria.

7. Blaha, P., Schwarz, K., Sorantin, P., Trickey, S.B., 1990. Improved version of Blaha, P., Schwarz, K., Sorantin, P. and Trickey, S.B. Comput. Phys. Commun. 59, 399.
8. Brockt, G., Lakner, H., 2000. Nanoscale EELS analysis of dielectric function and bandgap properties in GaN and related materials. Micron 31, 435–440.
9. Cheng-Zhang, L., Fey, G.T.K., 2006. Nanocrystalline and long cycling LiMn2O4 cathode material derived by a solution combustion method for lithium ion batteries. J. Phys. Chem. Solids 67, 756–761.
10. Egerton, R.F., 1996. Electron Energy Loss Spectroscopy in the Electron Microscope. Plenum Press, New York.
11. Fu, L.J., Liu, H., Li, C., Wu, Y.P., Rahm, E., Holze, R., Wu, H.Q., 2005. Electrodematerials for lithium secondary batteries prepared by sol–gel methods. Prog. Mater. Sci. 50, 881–928.
12. Grechnev, G.E., Ahuja, R., Johansson, B., Eriksson, O., 2002. Electronic structure, magnetic and cohesive properties of LixMn2O4: theory. Phys. Rev. B 65, 174–408.
13. Gurtubay, I.G., Ku, W., Pitarke, J.M., Eguiluz, A.G., Larson, B.C., Tischler, J., Zschack, P., 2004. Large crystal local-field effects in the dynamical structure of rutile TiO2. Phys. Rev. B 70, 201201.
14. Hwang, B.J., Santhanam, R., Liu, D.G., 2001. Effect of various synthetic parameters on purity of LiMn2O4 spinel synthesized by sol–gel method at low temperature. J. Power Sources 101, 86–89.

15. Jeong, S.K., Chi-Hoon, S., Nahm, K.S., Stephan, A.M., 2006. Synthesis and electrochemical properties of Li[Li0 07Ni0.1Co0.6Mn0.23]O2 as a possible cathode material for lithium-ion batteries. Electrochem. Acta 52, 885–891.
16. Kwang, J.K., Jang, H.L., 2007. Effects on nickel doping on structural and optical properties of spinel lithium manganate thin films. Solid State Commun. 141, 99–102.
17. Kuwata, N., Kumar, R., Toribami, K., Suzuki, T., Hattori, T., Kawamura, J., 2006. Thin film lithium ion batteries prepared only by pulsed laser deposition. Solid State Ionics 177, 2827–2832.
18. Mauchamp, V., Boucher, F., Ouvrad, G., Moreau, P., 2006. Ab initio simulation of the electron energy-loss near-edge structures at the Li K edge in Li, Li_2O, and $LiMn_2O_4$. Phys. Rev. B 74, 115106.
19. Mishra, S.K., Ceder, G., 1999. Structural stability of lithiummanganese oxides. Phys. Rev. B 59, 6120–6130.
20. Na, Y., Changlu, S., Yichun, L., Hongyu, G., Xinghua, Y., 2005. Nanofibers of $LiMn_2O_4$ by electrospinning. J. Colloid Interface Sci. 285, 163–166.
21. Rojas, R.M., Amarilla, J.M., Pascual, L., Rojo, J.M., Kovacheva, D., Petrov, K., 2006. Combustion synthesis of nanocrystalline LiNiYCo1"2YMn1+YO4 spinels for 5 V cathode materials: characterization and electrochemical properties. J. Power Sources 160, 529–535.
22. Siapkas, D.I., Mistas, C.L., Samaras, I., Zorba, T.T., Moumouzias, G., Terzidis, D., Hatzikraniotis, E., Kokkou, S., Voulgaropoulos, A.,

Paraskevopoulos, K.M., 1998. Synthesis and characterization of LiMn2O4 for use in Li-ion batteries. J. Power Sources 72, 22–26.

23. Singh, D.J., 1997. Magnetic and electronic properties of LiMnO2. Phys. Rev. B 55, 309.
24. Tang, S.B., Lai, M.O., Lu, L., Tripathy, S., 2006. Comparative study of LiMn2O4 thin film cathode grown at high, medium and low temperatures by pulsed laser deposition. J. Solid State Chem. 179, 3831–3838.
25. Tao, L., Weihua, Q., Hailei, Z., Jingjing, L., 2006. Effect of cooling rate on the electrochemical properties of solid-state synthesized spinel LiMn2O4. Mater. Lett. 60, 1251–1255.
26. Tu, J.P., Wu, H.M., Yang, Y.Z., Zhang, W.K., 2007. Spray-drying technology for the synthesis of nanosized LiMn2O4 cathode material. Mater. Lett. 61, 864–867.
27. Van der Ven, A., Marianetti, C., Morgan, D., Ceder, G., 2000. Phase transformations and volume changes in spinel LixMn2O4. Solid State Ionics 135, 21–32.
28. Vast, N., Reining, L., Olevano, V., Schattschneider, P., Jouffrey, B., 2002. Local field effects in the electron energy loss spectra of rutile TiO2. Phys. Rev. Lett. 88, 037601.
29. Wang, X., Chen, X., Gao, L., Zheng, H., Mingrong, J., Shen, T., Zhang, Z., 2003. Citric acid-assisted sol–gel synthesis of nanocrystalline LiMn2O4 spinel as cathode material. J. Cryst. Growth 256, 123–127.

30. Wu, H.M., Tu, J.P., Yuan, Y.F., Li, Y., Zhao, X.B., Cao, G.S., 2005. Structural, morphological and electrochemical characteristics of spinel LiMn2O4 prepared by spray-drying method. Scripta Mater. 52, 513–517.
31. Yun-Sung, L., Yang-Kook, S., Kee-Suk, N., 1998. Synthesis of spinel $LiMn_2O_4$ cathode material prepared by an adipic acid-assisted sol–gel method for lithium secondary batteries. Solid State Ionics 109, 285–294.